RESEARCH ARTICLE

An improved three-dimensional concentration measurement technique using magnetic resonance imaging

Andrew J. Banko[1] · Michael J. Benson[2] · Ian E. Gunady[3] · Christopher J. Elkins[1] · John K. Eaton[1]

Abstract

Magnetic resonance concentration (MRC) was introduced by Benson et al. (Exp Fluids 49:43–55, 2010) to obtain three-dimensional, time-averaged concentration fields in complex turbulent flows without the need for optical access using magnetic resonance imaging. It has since been applied to a wide variety of flows including jet engine film cooling configurations, mixing layers, and urban dispersion cases. However, the measurement uncertainty is currently limited to about 5% of the injected concentration, irrespective of the local concentration. This work presents an advanced MRC technique to greatly reduce the uncertainty at low concentration. Best practices for conducting MRC experiments are described to establish a baseline methodology. These include the choice of scan settings and fluids, calibration procedure, mixing experiment details, and method for computing concentration fields from scan data. An advanced technique is developed to reduce the uncertainty at low concentration by combining data from multiple experiments at increasing molarity of injected fluid, using Fourier-space averaging to reduce noise, and by minimizing fluid property differences using a low flip angle to reduce the maximum injected molarity without degrading the signal-to-noise ratio. The method is flexible and can be optimized to meet the uncertainty requirements of specific applications. Experiments are performed on the turbulent mixing downstream of an isolated, rectangular building as a test case. The advanced technique is validated against the baseline method and maps of spatially dependent experimental uncertainty are presented. Less than 1% uncertainty based on a 95% confidence interval is achieved near the plume boundaries. Results from the new technique reveal dilute but non-zero concentration regions near the wall which could not be resolved using the baseline method.

Graphic abstract

(a) Isosurface at 30% concentration.

(b) Isosurface at 2% concentration.
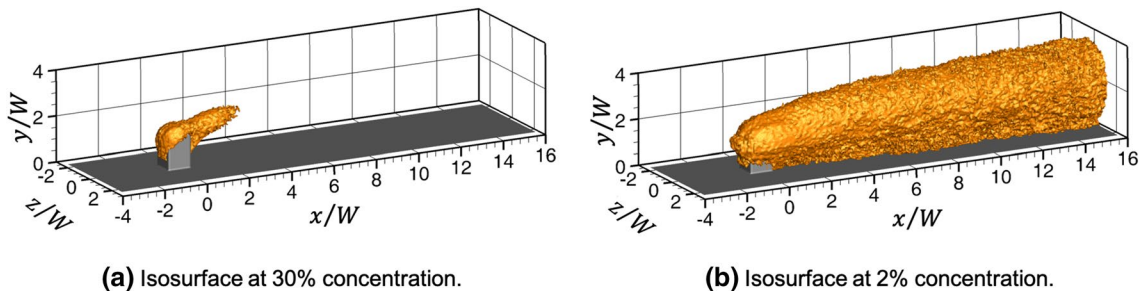
✉ Andrew J. Banko
   abanko@stanford.edu

1 Mechanical Engineering, Stanford University, Palo Alto, CA, USA

2 Mechanical Engineering, U.S. Military Academy, West Point, NY, USA

3 Mechanical and Aerospace Engineering, Princeton University, Princeton, NJ, USA

1 Introduction

Turbulent scalar mixing crosses many scientific disciplines, from human and environmental health to power generation. Fluid mixtures may consist of as few as two substances, such as salt in sea water, and as many as 100 may result from a relatively simple combustion event. In some flows, substances chemically react, are buoyant, or otherwise influence

the flow behavior. In other flows, the substances can be treated as passive scalars. Often significant insight can be gained by studying the two-component turbulent mixing. Examples include fundamental studies on turbulent transport (Dimotakis 2005), dispersion of noxious gases or pollutants in a city (Sini et al. 1996), advection of smoke from wildfires (Stein et al. 2015), and also heat transfer applications via analogy between temperature and scalar concentration (Bogard and Thole 2006). In all cases, concentration measurements are required for establishing physical understanding, validating computational models, or determining emergency response procedures. Therefore, the present work focuses on the measurement of scalar concentration in two-stream mixing applications.

Many different techniques for measuring concentration are available in the context of lab-scale studies in idealized geometries, component scale experiments for engineering design, and field tests. Devices for measuring the concentration of a species in a flow can be developed for something specific—such as for chlorine gas—or can be species agnostic, such as in some light or laser absorption techniques (Penner and Jerskey 1973; Cottereau et al. 1989). Rather than give a review of all available methods, a short list is provided of a few of the most common means. These techniques include isokinetic sampling probes, planar laser-induced fluorescence (PLIF), spectroscopic laser scattering, gas chromatography and analyzers, X-ray tomography, pressure sensitive paint, and more (Lozano et al. 1992; Crimaldi 2008; Escoda and Long 1983; Brockhinke et al. 1995; Golnabi 2006; Dunnmon et al. 2017; Zhang 1999). The techniques listed above share several major advantages and disadvantages. One advantage of some of these methods is the ability to provide time-resolved data and, therefore, access to turbulence statistics. Camera-based techniques can also achieve high spatial resolution. On the other hand, with the exception of X-ray tomography, most methods obtain data only at a point or on two-dimensional planes. PLIF has been used to collect three-dimensional data, but this increases experimental complexity, because the laser system must be scanned across the volume of interest. The optical techniques also often require two directions of optical access, which limits the complexity of geometries that can be studied.

Magnetic resonance imaging (MRI) has been used for about a decade in the investigation of concentration distributions in turbulent flows (Benson et al. 2010). The benefits of this technique—known as magnetic resonance concentration (MRC)—include the means to conduct highly detailed three-dimensional measurements without any optical accessibility requirements for a mixture originating from two fluid streams. MRC as developed measures the mean concentration field of a scalar contaminant in water. Data are obtained on a Cartesian array of voxels throughout an entire 3D

volume, and as such includes the effects of both molecular mixing and stirring (Dimotakis 2005). Therefore, turbulent mixing can be studied in highly complex geometries. Since its development, MRC has been used to measure a variety of engineering flows including shear layers (Benson et al. 2010; Yapa et al. 2014), trailing edge film cooling (Benson et al. 2011; Yapa et al. 2015), discrete hole film cooling (Coletti et al. 2013; Ryan et al. 2017; Borup et al. 2019), and dispersion in urban environments (Shim et al. 2019; Benson et al. 2019). It has also been used to validate and improve numerical simulations (Ling et al. 2013; Milani et al. 2019). The large 3D data sets provide a stringent basis for comparison between experiment and computation. Finally, MRC has been validated against more traditional experimental techniques including PLIF and temperature probe measurements (Benson et al. 2010; Yapa et al. 2014; Sayles and Eaton 2016).

Despite some obvious advantages over other techniques, several limitations have also been identified. The MRC method cannot measure statistics of turbulent concentration fluctuations. Transient measurements are currently limited to phase-averages in periodic flows (Borup et al. 2019). The Cartesian data matrix and voxel resolution also preclude wall-resolved concentration measurements in complex geometries. In some cases, the wall concentration can be extrapolated from the first voxel above the surface because of the no-flux boundary condition for the scalar contaminant. This has been demonstrated for film cooling measurements (Ryan et al. 2017; Milani et al. 2019). Since both fluids are water-based and the contaminant has dilute solutions of a paramagnetic substance, slight density differences exist between the two fluid streams. Finally, the measurement uncertainty is consistently around 5% of the injected concentration. Very dilute concentrations are of particular interest in urban and environmental applications, where even small concentrations of certain chemicals can pose life hazards.

The purpose of the present work is threefold. First, current best practices for conducting MRC measurements are explained in detail. These practices include details regarding scanner settings, experimental set-up, and data processing. Second, the results from an alternative set of scan parameters are validated against the baseline method, which may have utility in applications where density and other fluid property effects must be minimized. Third, a technique to greatly reduce the measurement uncertainty at low concentration is described. Overall, a comprehensive understanding of the capabilities of the technique is expected to provide greater accessibility to other studies that can benefit from MRC.

2 Experimental set-up

Measurements of scalar dispersion are made in the wake of an isolated building. The flow geometry is depicted in Fig. 1. The building model has a 10 mm × 10 mm square footprint and is 15 mm tall, giving a height-to-width ratio ($H:W$) of 3:2. Scalar contaminant is injected through rectangular arrays of holes on the upstream and downstream faces. These holes are 0.9 mm in diameter, 2.8 mm long, and inclined at 45° with respect to the floor of the test section. Each hole is fed from the interior of the building which is hollow and has a tapered divider to improve the uniformity of the flow distribution between holes. The divider begins at the upstream edge of the first row of holes and has a rounded leading edge, with a 0.25 mm radius of curvature, to prevent the flow from separating in one of the passages. The divider tapers each passage down to a minimum gap of 0.25 mm and extends 0.8 mm past the downstream edge of the last row of holes, so that manufacturing imperfections do not create blockages in these holes. The flow passage upstream of the divider has a 6 mm × 6 mm square cross-section.

The building is centered within the test section, which has a 49.8 mm × 49.8 mm square cross-section. The main flow enters the test section through a flow conditioning section consisting of a gridded diffuser, a settling chamber with honeycomb and grid, and a 4:1 contraction. A boundary layer trip on all four walls initiates a new turbulent boundary layer

210 mm upstream of the center of the building. The flow conditioning pieces, test section, and building injector were 3D printed using stereolithography at the W.M. Keck Center (University of Texas at El Paso).

De-aerated water was used as a working fluid with copper sulfate ($CuSO_4$) added in varying concentrations as a contrast agent to study the scalar mixing. The choice of $CuSO_4$ molarity is discussed in Sect. 3. The main flow was operated at a bulk velocity of 0.3 m/s, which corresponds to a Reynolds number of $Re_W = 3000$ based on the building width and properties of water at 20 °C. The Reynolds number based on the distance of the trip location to the building center is $Re_x = 64{,}000$. The injection flow rate through the building was chosen to give a bulk velocity of 0.39 m/s through each hole, assuming uniformly distributed flow. This yields a blowing ratio of 1.3, defined as the ratio of injection to main flow bulk velocities. Note that the flow rates through the upstream and downstream faces were not actively controlled. It is therefore expected that less flow exits on the upstream side where the stagnation pressure is higher. The flow conditions were chosen such that the wake is turbulent, and the blowing ratio of contaminant is in a regime relevant to smoke emanating from a burning building under typical wind speeds. The inclined holes provide a component of vertical momentum to emulate the net effect of a buoyancy-driven flow. However, the primary purpose of the geometry was to demonstrate a new MRC technique as opposed to
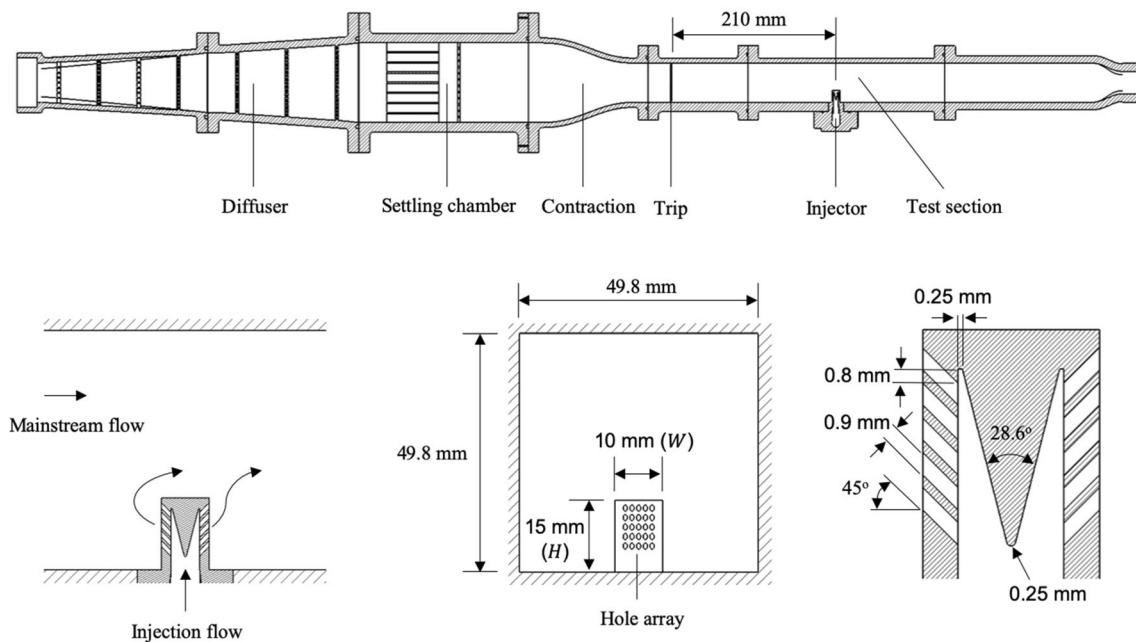

Fig. 1 Building injector and channel geometries. Top: apparatus including upstream components and test section. Bottom left: streamwise parallel cross-section through the center of the injector. Bottom center: streamwise-normal cross-section showing upstream face of the building with hole array. Bottom right: injector cross-section

matching all relevant dimensionless parameters related to problems of smoke dispersion.

Experiments were performed at the Richard M. Lucas Center for Imaging at Stanford University using a General Electric (GE) Discovery MR750 3.0 Tesla MRI system and a transmit and receive coil typically used for imaging human heads. The flow conditioning inlet and test section outlet were connected to a series of tanks located inside the magnet room and outside the building. The in-room tanks were a small reservoir with main or injection flow supply and filled with the $CuSO_4$ solution, a large reservoir with main or injection flow supply and filled with water, and an auxiliary reservoir to provide capacitance when pumping fluid to the outside tank farm. The outside tank farm consisted of six 1000-L reservoirs to mitigate contamination of the water by mixed fluid exiting the test section. Two additional reservoirs were located outside to hold high-concentration waste fluid. The tank farm and large reservoir temperatures were not actively controlled, but their large thermal inertia resulted in a near constant temperature of approximately 20 °C over the duration of the experiment. The small reservoir temperature was monitored using a thermometer and maintained at 20 °C using a cooling coil fed by the building's chilled water supply. A scale was placed under the small reservoir. This was used to determine the total volume of water of the reservoir, feed lines, and the channel, which is needed to calculate the concentration of $CuSO_4$ during the calibration procedure as discussed in Sect. 3.2.3.

The main flow was supplied by a 0.37 kW (1/2 hp) pump (Little Giant model TE-6-MD-HC) and the injected flow was supplied by a 0.09 kW (1/8 hp) pump (Little Giant model 5-MD-SC). Both main and injection flow rates were monitored using Transonic PXL Flowsensors and controlled using diaphragm and needle valves, respectively. Depending on the scan, the main and injection flows individually drew from either the small reservoir or the large reservoir as set by T-junctions upstream of both pumps. The pump outlets were routed to the channel by flexible tubing. The flow out of the test section was routed either to the small reservoir, large reservoir, or capacitance tank using flexible tubing. Flow from the capacitance tank was pumped to the tank farm or waste tanks using a 0.56 kW (3/4 hp) pump (Little Giant model TE-7-MD-SC) controlled with a diaphragm valve and monitored with a paddle wheel flow meter. Flow was pumped from the tank farm and back into the large reservoir using a 0.75 kW (1 hp) pump (Berkeley model BPHD10-L) controlled with a diaphragm valve and monitored with a paddle wheel flow meter. The flow loop is shown in Fig. 2, and the reader can find more detailed descriptions of the flow loop, including diagrams, in Yapa (2015) and Ryan (2016).

Fig. 2 Diagram of the flow loop within the magnet room
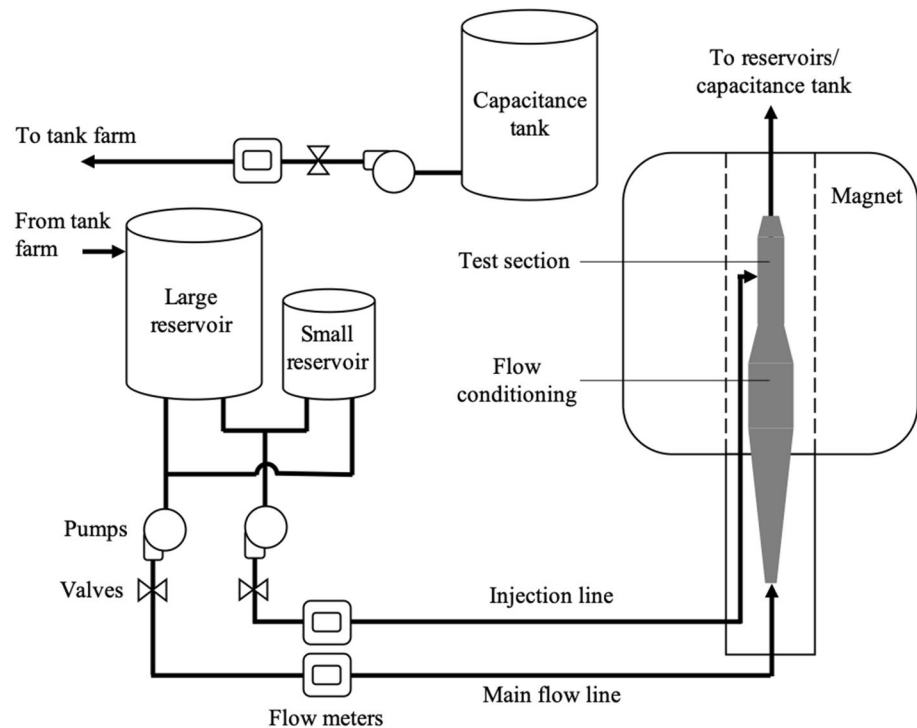
3 Magnetic resonance concentration

3.1 Fundamentals

MRI systems image the spatial distribution of nuclear magnetic spins (e.g., hydrogen protons in water). A brief description of the principles is given here, and the reader is referred to Haacke (1999), Nishimura (2010), and Elkins and Alley (2007) for a comprehensive treatment of basic physics, scan sequences, imaging artifacts, and flow applications.

In the presence of a static magnetic field, a fraction of the spins align with the field. A radio frequency (RF) pulse is used to flip a volume of spins out of alignment (excitation). The tipped spins precess about the axis of the main magnetic field at the Larmor frequency. This generates time-varying transverse magnetization which is detected as radio waves during readout, called an echo. The longitudinal component regrows, and the transverse component decays exponentially over time at the relaxation rates $1/T_1$ and $1/T_2^*$, respectively. The Larmor frequency is a linear function of the magnetic field strength, so the spatial locations of spins are encoded by applying magnetic field gradients during excitation and readout when spin signals are measured (Haacke 1999). The time between excitation and the center of the readout is called the echo time (TE), and the time between excitations is called the repetition time (TR). These parameters can depend on the sampling rate, gradient magnitudes, gradient slew rate, and desired spatial resolution. They also depend on additional details of the pulse sequence such as a gradient spoiling step or partial k-space readout.

The echo and magnetization magnitude form a Fourier transform pair as a result of phase encoding (Nishimura 2010). By sampling the Fourier domain (k-space) over repeated excitations and readouts, the image is reconstructed via the inverse Fourier transform. A Cartesian sampling pulse sequence was used to acquire k-space on a Cartesian grid. Precise specification of the pulse sequence timing is beyond the present scope and the reader is referred to Elkins and Alley (2007) for more detail.

MRC exploits the dependence of the signal magnitude on the concentration of a contrast agent added to the fluid. The signal magnitude depends on the type of fluid, fluid motion, flip angle, relaxation rates, TE, TR, and amplifier gains; and a contrast agent modifies the relaxation rates $1/T_1$ and $1/T_2^*$ (Haacke1999). This dependence is linear over a range of contrast agent molarities and for short TE and TR, as verified by in situ calibration (Schenck 1996; Haacke 1999).

3.2 Baseline MRC method

Current best practices for conducting MRC experiments and processing data were derived from experience by the authors and others in applying MRC to a variety of engineering flows. In what follows, a coordinate system is defined with the origin located at the base of the building and centered within its horizontal cross-section. The streamwise direction is x, y is the wall-normal direction (e.g., parallel to the building height), and z is the spanwise direction. All lengths are normalized using the building width, W.

3.2.1 Fluid pair selection

Water and an aqueous $CuSO_4$ solution were chosen, because they provide a balance between the dynamic ranges of the measurement, accessible operating conditions (e.g. Reynolds number), cost, ease of use, and waste disposal requirements. A large volume of fluid was needed in the present experiments: 6000 L of water in the tank farm and 60 L of $CuSO_4$ solution for a single reference concentration. Although the volume can be reduced for experiments with smaller flow rates, this still precludes the use of other fluids such as deuterium oxide (heavy water) and hyperpolarized gases. Figure 3 plots the relaxation rates as well as the density and kinematic viscosity ratios of $CuSO_4$ solutions to pure water for varying molarities (Schenck 1996; Parmar and Thakur 2006). The viscosity is most affected by the addition of $CuSO_4$. However, for most turbulent flows of engineering interest, the Reynolds number is large enough that the turbulent transport away from solid boundaries is not sensitive to viscous effects. The Schmidt number for $CuSO_4$ in water is $O(1000)$, indicating that the molecular diffusion of concentration is negligible.
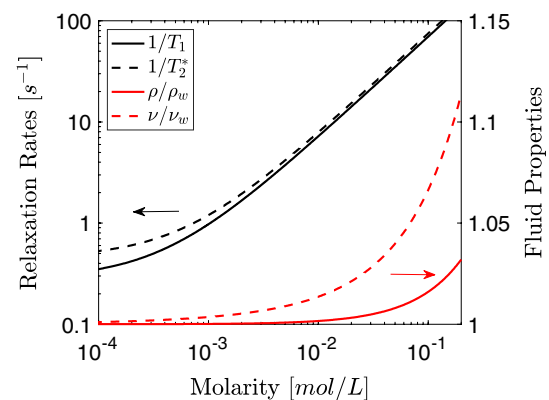

Fig. 3 Relaxation rates and fluid properties of a $CuSO_4$ solution for varying molarity. Relaxation rates are taken from Schenck (1996) for a 1.5 T magnetic field and at 25 °C. Fluid properties ratios are relative to pure water at 25 °C and taken from Parmar and Thakur (2006)

3.2.2 Scan settings

A 3D fast spoiled-gradient echo sequence was used with sagittal slice planes (spanwise-normal planes). The frequency (readout) direction was aligned with the *x*-axis of the channel. A partial *k*-space readout was used to reduce the scan time. Only 60% of the k_x data were sampled, such that $k_x \in \left[-0.2k_{x,\max}, k_{x,\max}\right]$, where $k_{x,\max}$ is the maximum wavenumber in the *x*-direction. Two flip angles were considered. The baseline configuration was 55° (Flip55) and has been used across a variety of flow configurations. An alternative configuration at a lower flip angle of 30° (Flip30) was also studied. The purpose of the alternate setting was to investigate the use of low flip angle for quantitative measurements, because it allows the advanced technique developed in Sect. 4 to be extended to a wider range of conditions.

Table 1 reports the scan settings for each case. Row 1 includes scan settings that are specific to the geometry. The field of view (FOV) was 25.6 cm × 9.2 cm × 6.24 cm in the streamwise, spanwise, and wall-normal directions; the imaging matrix was 384 × 138 × 104 elements in size; and the voxel resolution was 0.6 mm in each direction. The FOV was chosen to contain all fluid regions in the phase encode and slice directions, and to place the edges of the FOV far from the region of interest where the signal can be affected by inflow effects and image shading (Nishimura 2010). Row 2 reports additional scan parameters, including TE and TR which depend on flip angle. The resulting scan time for the baseline case was 1 min 56 s. The data matrix for the Flip30 case was the same as for the Flip 55 case, but TR was slightly different, and the resulting scan time was shorter at 1 min 43 s.

Pre-scan settings which include system gains were obtained with the channel filled with fluid at the reference concentration and moving at the desired flow rate. The reference concentration was chosen after a detailed calibration described in the next section. It should be noted that TE, TR, and the pre-scan channel settings are dependent on the FOV, channel size, reference concentration, and flip angle. It is crucial to hold these values constant across all scans to accurately calculate the concentration field.

3.2.3 Calibration

A calibration experiment was performed to determine the linear range and reference concentration for injection. A linear relationship is required so that the concentration inferred from the measured signal magnitude is unbiased for flows with concentration fluctuations due to turbulent mixing. If the calibration is a non-linear function of concentration, then the mean signal magnitude measured by MRC will not be equal to the signal magnitude at the mean concentration. Calibrations are required for each new channel geometry and flow condition, because the linear range can depend on the experimental details. Initial scan settings are chosen based on prior experience and the approximate linear range is identified by completing a series of scans with a uniform concentration fluid flowing through the entire channel (both injection and main flow) at the experimental flow rate. The first scan uses pure water, followed by scans at increasing concentrations of $CuSO_4$. The $CuSO_4$ solutions are made by mixing several liters of pre-prepared high molarity solution into the small reservoir. The required volume of high molarity solution is calculated based on the volume of fluid in the small reservoir, lines, and channel. At the start of the experiment, the small reservoir is filled with a volume of water which is measured using a scale placed under the reservoir. The tubing, pumps, and channel are filled with this water, and subsequent additions of high molarity solution to the flow loop are recorded. Therefore, the volume and molarity of the fluid in the flow loop is known at every concentration level in the calibration.

Following the initial calibration, the scan settings such as flip angle, amplifier gains, and scanning domain are fine-tuned with $CuSO_4$ solution near the high end of the linear range (e.g., near the reference concentration), and the calibration is repeated. All calibration scans are performed with the flow on, because flow-dependent imaging artifacts that might impair signal linearity can be identified, and the flip angle or concentration range can be selected to minimize artifacts.

Figure 4 compares calibration curves for the Flip55 and Flip30 cases. Each point was obtained by averaging the signal magnitude over a common volumetric region of interest in the wake of the building for a single scan

Table 1 Scan settings for the building geometry

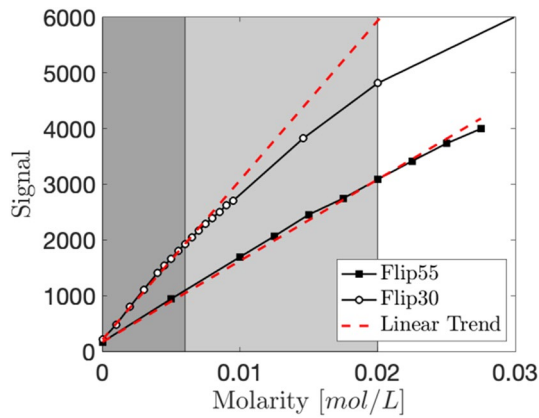| FOV (cm)	# of frequency elements	# of phase encodes	# of slices
25.6	384	138	104
Bandwidth (MHz)	**Echo time (TE) (ms)**	**Repetition time (TR) (ms)**	**Flip angle (°)**
31.25	1.7	9.4	55
	1.4	8.2	30

Fig. 4 Calibration data for 55° and 30° flip angle cases. Signal magnitude (arbitrary units) is plotted against the molarity of the $CuSO_4$ solution. The grayed regions mark the approximate linear range for each scan type, and the red dashed lines are the linear trends passing through 0 M and the reference concentration
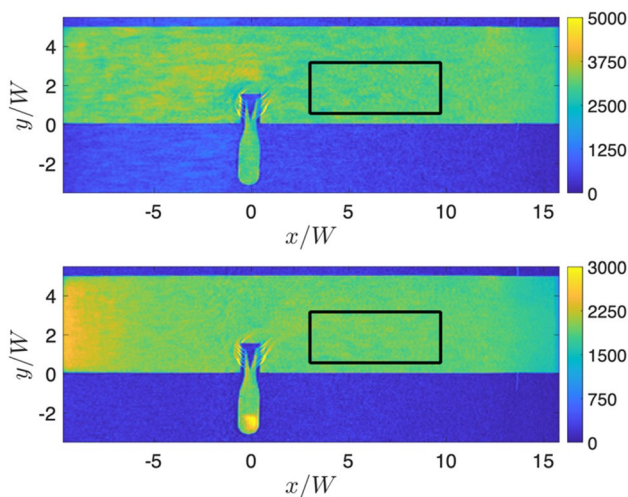

Fig. 5 Reference scans for flips angles of 55° (top) and 30° (bottom). Signal magnitude contours are plotted on the $z/W = 0$ plane. Note that the entire channel contains the reference concentration (both injection and main flow). The region of interest used to generate the calibration curve is outlined in black

(see Fig. 5). The curves are nearly linear over a range of concentrations and then decrease in slope as the concentration is increased further. Both the extent of the linear range and the dynamic range of the measurement increase with increasing flip angle. The reference concentrations for the Flip55 and Flip30 cases were identified as $M_{ref} = 0.02$ M and $M_{ref} = 0.006$ M, respectively. The dashed lines in Fig. 4 show the linear trend passing through 0 M and the reference concentration, which is the assumed linear relationship for computing concentration. The relative deviation of the linear assumption from the calibration data was

less than 3.5% for both flip angles, with the maximum occurring near the middle of the linear range.

The region of interest should not contain image artifacts, and the large region of interest was chosen to reduce noise in the calibration curve. The results are not sensitive to the particular choice of the region of interest. Although the slope can vary mildly with position due to image shading, for example, the extent of the linear range is consistent. The concentration fields are also determined using a pointwise processing method described below, so the final results are insensitive to spatial variations in the calibration.

The baseline scan settings were chosen from the calibration scans considering multiple factors. The high flip angle achieves the largest dynamic range without significantly affecting the fluid properties. Figure 3 shows that the density difference between 0.02 M $CuSO_4$ solution and water is negligible, and that the change in viscosity is less than 3%. Certain imaging artifacts are also reduced in this geometry at high flip angle. Figure 5 shows contours of signal magnitude at the reference concentration for each flip angle. Ideally, these fields would be perfectly uniform, but both cases contain image artifacts near the building, especially around the injection holes. The main difference between the cases is an increase in the inflow effects at low flip angle as seen in the region $x/W < -5$ and at the bottom of the injector. Spins entering the field of view have not yet been fully excited, and, therefore, their transverse magnetization requires several excitations to decay to steady state. This translates into an advection distance for moving spins. The number of excitations needed to reach steady-state decreases with increasing flip angle (Haacke 1999). Therefore, higher flip angles are also advantageous for experiments with faster flow.

3.2.4 Scans, data reconstruction, and concentration calculation

Concentration fields were computed from reference, background, and standard scans as outlined in Benson et al. (2010). Inverted scans were not used in the present work. Inverted scans reduce bias from Gibbs ringing in regions of the flow where the signal jumps from low to high values, such as for high-concentration fluid next to a wall (Benson et al. 2010; Nishimura 2010). Elsewhere, inverted scans only increase the measurement uncertainty, because noise is greater when the average signal in the channel is higher, i.e., when the main flow is at the reference concentration.

During reference scans, the entire apparatus was filled with the reference $CuSO_4$ concentration and both the main and injection flows were supplied from the small reservoir. The channel was operated with pure water during background scans. Finally, standard scans were completed by pumping pure water from the large reservoir through the main channel and the reference concentration of $CuSO_4$

from the small reservoir through the injection line. The mixed fluid was pumped out to the tank farm to dilute the concentration before it recirculated back to the large reservoir. The contamination of the main flow during standard scans was less than 1% of the linear range, and, therefore, had a negligible effect on the uncertainty.

A total of 20 repetitions were completed for each of reference, background, and standard scans to obtain the mean concentration field. In what follows, a single scan refers to the complete acquisition of k-space data to reconstruct a magnitude image. A single scan set refers to the collection of 20 scans of one type (e.g., reference, background, or standard). The apparatus was not moved throughout the entire experiment, so that the voxels from each scan were precisely aligned. Data acquisition in MRI is fundamentally different from optical and probe-based techniques that obtain spatially resolved, instantaneous data. Each scan acquires thousands of lines of k-space data over a period of about 2 min, where every k-space line contains non-local information from the entire FOV. Therefore, the entire flow field is effectively sampled thousands of times over a period that is much longer than all relevant flow time scales. The magnitude image from a single scan resembles the mean concentration field with predominantly large-scale statistical noise. As a result, only tens of these scans are required to reduce statistical errors as discussed in the next section.

The raw k-space data were reconstructed to obtain signal magnitude images. Uncollected k-space data from the partial readout were filled-in using a homodyne correction (McGibney et al. 1993), which corrects for non-linear phase variations to enforce conjugate symmetry in the Fourier coefficients. Because the symmetrically sampled data are limited in k-space, the phase corrections are expected to be less accurate very near the building where the phase varies more rapidly in space.

The concentration for each standard scan was calculated as:

$$C_i\left(\vec{x}\right) = \left(S_i\left(\vec{x}\right) - \sigma_{b,i}\overline{B}\left(\vec{x}\right)\right) \Big/ \left(\sigma_{r,i}\overline{R}\left(\vec{x}\right) - \sigma_{b,i}B\left(\vec{x}\right)\right), \tag{1}$$

where R, B, and S are the magnitude images from reference, background, and standard scans, respectively. The subscript i denotes each standard scan, the overbar indicates an average over all scans in a set, and $\sigma_{b,i}$ and $\sigma_{r,i}$ are background and reference scale factors for the ith standard scan, respectively. Subtraction of the background and normalization by the difference between reference and background account for spatial variations in signal magnitude due to non-idealities such as receiver coil sensitivity. The result is a 3D concentration field in the range of zero to one, where zero corresponds to pure water and one corresponds to the reference concentration of $CuSO_4$.
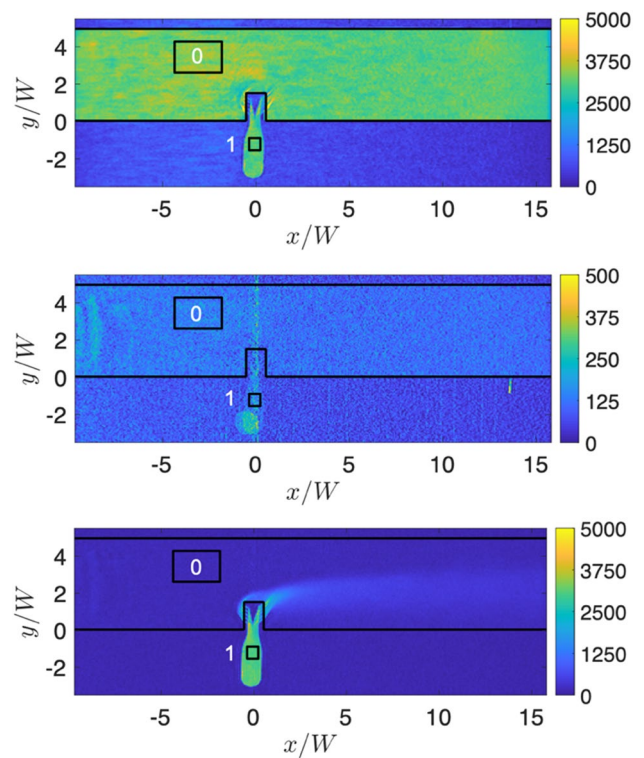

Fig. 6 Contours of signal magnitude for each scan type. Data are shown for the Flip55 case on the $z/W = 0$ plane. In order from top to bottom: reference, background, and standard. Note the change in scale for the background scan. Scaling ROIs are outlined by the black boxes. The channel walls are shown in black lines

The scale factors account for changes in the signal magnitude due to hardware drift over the course of the experiment and for slight contamination of the mainstream flow by the $CuSO_4$ added to the tank farm. For example, the overall signal may increase during the first couple scans of a given set as the scanner hardware heats up. In practice, the drift is small, because several scans are performed and discarded before data are kept to bypass this transient. The scale factors were computed via:

$$\sigma_{b,i} = \sum_{\text{ROI,0}} S_i \Big/ \sum_{\text{ROI,0}} \overline{B}, \tag{2}$$

and

$$\sigma_{r,i} = \sum_{\text{ROI,1}} S_i \Big/ \sum_{\text{ROI,1}} \overline{R}. \tag{3}$$

The summations are taken over all points in two volumetric regions of interest (ROI). ROI, 0 is taken in the freestream where the concentration is zero, and ROI, 1 is taken in the injector where the concentration is unity. Therefore, $\sigma_{b,i}$ scales the mean background image, so that the pure

water upstream of injection for ith standard scan has a concentration of zero on average. For instance, if contamination increases the signal from regions nominally containing pure water by 2%, then the background image should be scaled accordingly to compensate for this effect. Similarly, $\sigma_{r,i}$ scales the mean reference image, so that the reference fluid in the injector for the ith scan has a concentration of unity on average. Figure 6 shows the averaged reference, background, and standard scans with the ROI locations for the Flip55 case. It is important to locate the ROIs away from any image artifacts. ROI, 0 is placed upstream of injection, because the freestream fluid downstream of injection will be contaminated by noise which spreads non-locally in y–z planes despite the fact that the concentration is nominally zero. It was found that almost all scale factors differed from unity by less than 3%. Finally, all 20 concentration fields were averaged together. The result was a concentration field that was nominally unity in the injector and zero in the main flow upstream of injection, with statistical variations about these values.

Note that the calibration curve is not needed to compute the concentration, because the measurements are made in the linear range of the calibration curve. Instead, Eq. (1) is self-contained in the sense that the concentration is determined by comparing the measured signal magnitudes of the standard, reference, and background scans. Although precise knowledge of the fluid molarity is not required, care should be taken to ensure that the equipment and fluid preparation procedures are consistent between the calibration and measurement experiments, so that large systematic errors in fluid molarity are not introduced. Then, the accuracy of the concentration field is ultimately dependent on the accuracy of the signal measurements.

3.2.5 Uncertainty

The measurement uncertainty was quantified statistically by analyzing variations across the 20 concentration fields obtained via Eq. (1), similar to the method employed by Ryan (2016). The variance in concentration was calculated at each point in the FOV and Student's t distribution was used to assign a 95% confidence interval. This gives a spatial map of uncertainty. A typical value of uncertainty downstream of the building was 5% of the injected concentration and did not depend significantly on the local concentration. This level of uncertainty is representative of a wide variety of flows studied with the baseline MRC method, and has been corroborated by comparison to PLIF experiments (Benson et al. 2010), thermocouple measurements (Yapa et al. 2014; Sayles 2016), and highly resolved large eddy simulations (Ryan et al. 2017; Milani et al. 2019).

The statistical method accounts for thermal noise, dephasing, and turbulent fluctuations in the plume. Therefore, the uncertainty is higher near injection due to turbulent dephasing, in regions where the signal magnitude is high, and where the concentration fluctuations are large. Note that the uncertainty is roughly uniform within the channel cross-section, because these sources of uncertainty disperse noise non-locally in the phase encode and slice directions.

Additional uncertainties or biases can arise that are not accounted for by the statistics-based procedure. Examples include regions of strong flow acceleration due to spin misregistration, locations with excessive turbulence due to signal loss, and near the FOV boundaries due to inflow effects or coil sensitivity-induced shading. Voxels near solid boundaries also have increased uncertainty because of partial volume effects (Elkins and Alley 2007), artifacts induced by magnetic susceptibility differences (Schenck 1996), or phase errors not corrected by the homodyne reconstruction. These sources of uncertainty are more difficult to quantify, are localized in space, and highly dependent on the MRI hardware and flow geometry. Finally, uncertainties associated with the flow rates are negligible. The flow meters were calibrated prior to the experiment with repeatability errors of less than 1%, so that turning off the pumps between scan sets does not introduce additional uncertainty. The flow rates are also monitored during the scans and valves are adjusted as needed to maintain the flow rate within 2% of the nominal value.

4 Advanced MRC method

The noise floor of the baseline method makes it difficult to distinguish low concentration regions from freestream fluid in the far wake of the building, which can be important in urban dispersion and other turbulent mixing applications. The goal of the advanced MRC technique is to reduce the measurement uncertainty at low concentration by an order of magnitude to extend the dynamic range and resolve low concentration isosurfaces of the plume. Averaging over additional scans is an impractical solution. For example, a $5\times$ reduction in uncertainty requires approximately 25 times the number of scans for each of reference, background, and standard, since all scan types contribute to the uncertainty (c.f. Ryan 2017). This translates to 50 h of continuous scanning as opposed to 2 h for the baseline method.

An alternative approach is to increase the injected molarity and analyze mixing downstream where the $CuSO_4$ concentration falls within the linear range. The uncertainty is reduced, because the noise floor remains a fixed percentage of the linear range, but the linear range is now a fraction of the injected concentration. The advantage of this approach is that the number of scans scales linearly instead of quadratically with the desired level of uncertainty.

The advanced MRC method improves the baseline method using this approach via the following steps:

1. An MRC is completed using the baseline methodology.
2. A second set of scans injecting high molarity $CuSO_4$ solution are conducted.
3. The high molarity data are matched with the baseline data in an overlap region and the data sets are blended (stitched), thereby reducing uncertainty in dilute regions of the plume.
4. The above procedure is repeated by increasing the injection molarity until the desired level of uncertainty is achieved.

Three new components are introduced and described in the following sections: a high molarity scan procedure, a new averaging method to eliminate dephasing artifacts worsened by the increase of signal magnitude in the channel, and a method for stitching the data from the baseline and high molarity scans. A disadvantage of the new technique is that increasing the concentration of $CuSO_4$ beyond 0.3 M can produce important property differences with respect to water (c.f. Fig. 3). Magnetic susceptibility differences also become significant in excess of 0.3 M and lead to signal loss (Schenck 1996). These limitations are mitigated using a low flip angle. A low flip angle increases the signal for a given concentration, so that lower molarity fluid can be injected without substantial loss of dynamic range.

4.1 Validation of low flip angle scans

Results from the Flip30 parameter set are first validated against the Flip55 case. Figure 7 plots contours of concentration and uncertainty on the $z/W = 0$ plane for each flip angle. The concentration distributions are in close agreement downstream of injection. Some differences are observed around the injection holes and are likely the result of imaging artifacts. The uncertainty contours indicate that the level of noise is higher at low flip angle than at high flip angle. The concentration distribution extends further upstream and extends a shorter distance directly above the building for the Flip55 case. This was due to an unintended change in the flow condition during standard scans. Examination of the 3D concentration distribution showed increased feed around the negative z-side of the building. The Flip30 case and additional scans performed at higher molarity for both flip angles (described in the sections below) did not show this asymmetry.

Figure 8, which includes vertical profiles along $z/W = 0$ and spanwise profiles along $y/W = 1.5$, quantitatively compares concentration profiles for each flip angle. The shaded bands represent median filtered 95% confidence intervals computed using the statistical method. Results from each flip angle agree to within experimental uncertainty at almost all points in the profiles. The only exceptions are near injection due to the asymmetric feed as described above. The first vertical profiles show a discrepancy around $y/W = 2$. The asymmetry is also observed in the Flip55 spanwise profiles. The concentration distribution peaks on the negative z-side of the building and decreases towards the positive z-side. With the exception
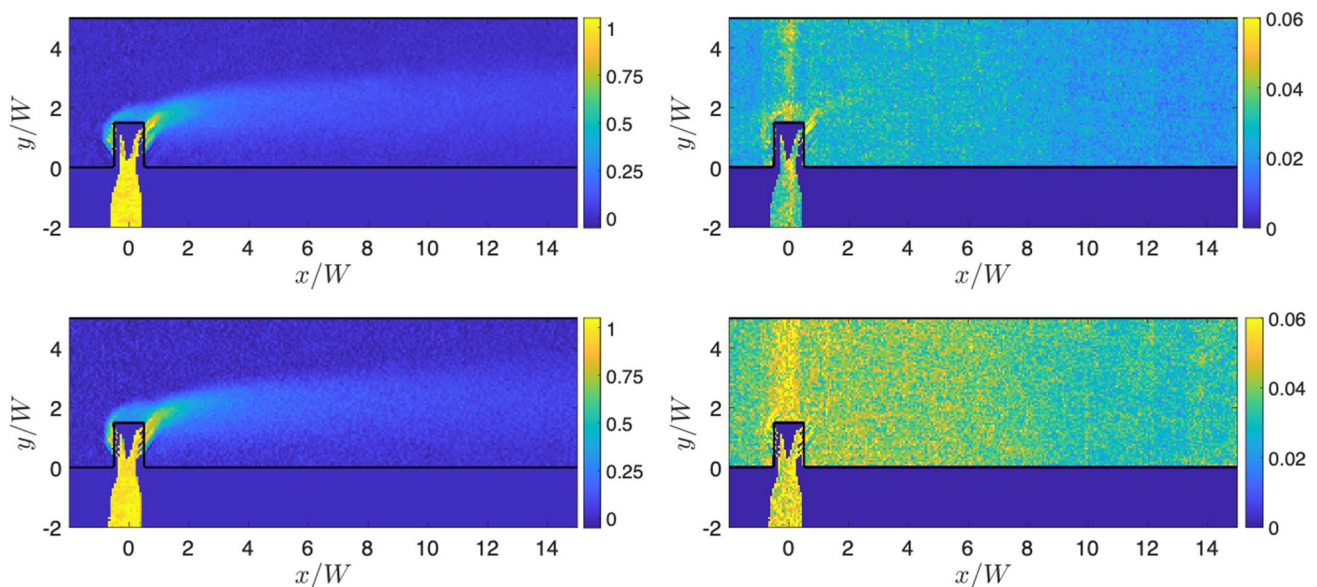

Fig. 7 Concentration (left) and uncertainty (right) contours at the $z/W = 0$ plane for flip angles of 55° (top) and 30° (bottom)
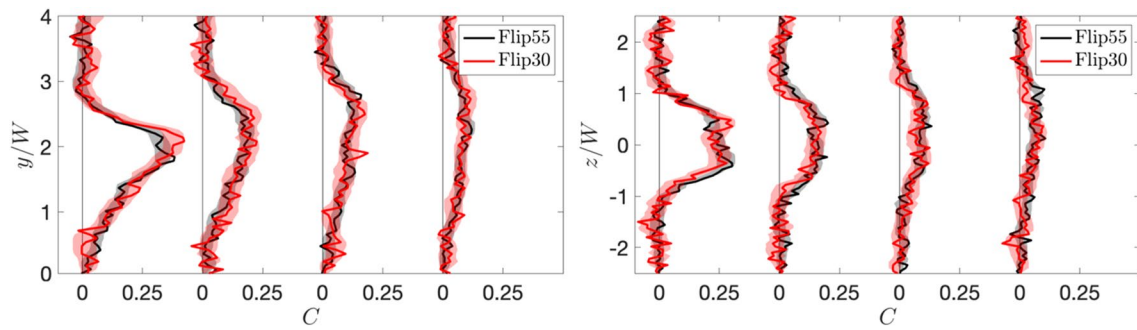
Fig. 8 Line plots of concentration for each flip angle at the streamwise positions $x/W = 2, 4, 8,$ and 12. Vertical profiles in the $z/W = 0$ plane are shown on the left, and spanwise profiles in the $y/W = 1.5$ plane are shown on the right. Shaded bands denote 95% confidence intervals

of these flow-related differences, the low flip angle data are in good agreement with the baseline MRC method and we conclude that the low flip angle parameter set can be used quantitatively.

4.2 High molarity scans

The high molarity scans were conducted using the same experimental set-up as for standard scans. High molarity fluids at 5 times and 25 times the original reference concentration were injected from the small reservoir and pure water was pumped to the main channel from the large reservoir. These are termed standard-high and super-high scans, respectively. The standard–high concentration was selected so that the linear range covers up to 20% of the injected concentration. This reduces the uncertainty while retaining an overlap range of concentration that can be accurately measured using standard scans to stitch the data sets (c.f. Sect. 4.4 below). The super-high concentration was selected using a similar argument applied to the standard–high scans. Other molarities could be selected depending on the flip angle chosen, acceptable levels of fluid property differences, and a desired level of uncertainty over a target range of concentrations.

Sets of 20 standard-high and super-high scans were performed for the Flip30 case. One set of 20 standard-high scans were performed for the Flip55 case. Super-high scans were not used at high flip angle because of the substantial fluid property differences. The mixed fluid was circulated to the tank farm during standard–high scans in the same way as for standard scans. The extra contamination increased the signal in the mainstream flow by 5% of the linear range over the course of the scans. This level of background drift does not introduce a measurable bias in the concentration field when appropriately accounted for via scale factors (see Sect. 3.2.4). During super-high scans, the mixed fluid was pumped to the waste reservoirs and not recirculated into the mainstream flow.
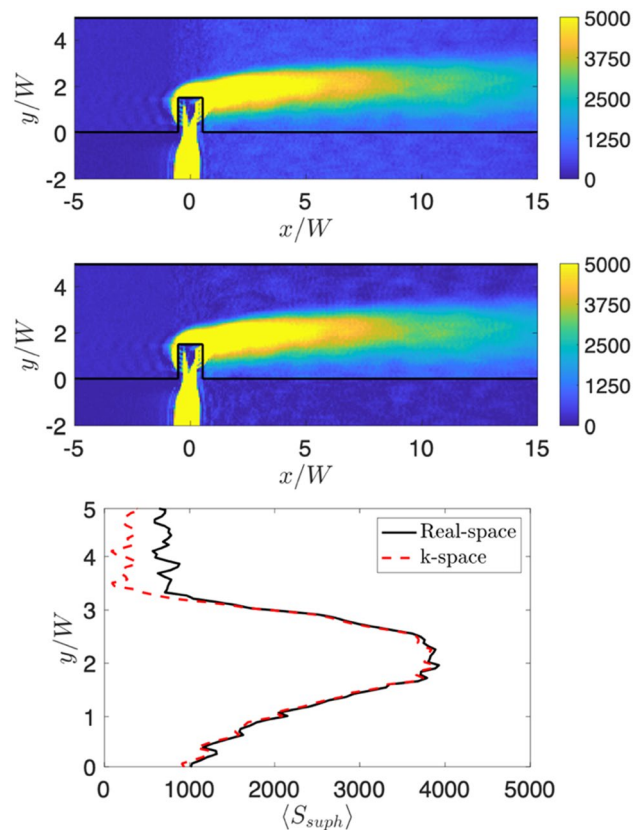

Fig. 9 Comparison of averaging techniques: contours of signal magnitude at the $z/W = 0$ plane when scalar magnitude scans are averaged (top), and k-space data are averaged prior to reconstruction (middle). The bottom figure shows line plots of the same data at $x/W = 4$. Data are for the super-high scan at 30° flip angle

4.3 *K*-space averaging

Concentration fields were obtained for the original processing method by reconstructing magnitude images and then averaging the physical-space data. Applying the same procedure to standard-high and super-high scans results in artificially increased freestream magnitude downstream of

injection as shown in the top contour plot in Fig. 9. This is due to the same noise sources present in standard scans, but the effect is exacerbated by the overall increase in signal within the channel. The result is that the concentration is biased to positive values in the freestream.

Noise in MRI is rectified when the magnitude image is reconstructed (see Nishimura (2010) for a discussion of Rician noise). This bias was reduced by averaging each set of scans in k-space prior to reconstruction (e.g., averaging the Fourier coefficients). The result is shown in Fig. 9. The mean value of the signal decreases in the freestream where the concentration is known to be zero. Large-scale noise still exists due to turbulent fluctuations in the plume, but the noise no longer acts as a bias when the concentration field is calculated. The line plot shows that the signal at $y/W = 0$ was previously indistinguishable from the signal in the range $y/W > 3$, and that $CuSO_4$ is detected at the wall with k-space averaging.

The analog of Eq. (1) for computing concentration with k-space averaging is:

$$\langle C_\alpha \rangle = \left(\overline{\sigma}_{r,s} \langle R \rangle - \overline{\sigma}_{b,\alpha} \langle B \rangle \right)^{-1} \left(\langle S_\alpha \rangle - \overline{\sigma}_{b,\alpha} \langle B \rangle \right.$$
$$\left. + \varepsilon \left(\left\langle \sigma'_{b,\alpha} S_\alpha \right\rangle - \overline{\sigma'^2_{b,\alpha}} \langle B \rangle \right) + \varepsilon^2 \left(\left\langle \sigma'^2_{b,\alpha} S_\alpha \right\rangle - \overline{\sigma'^2_{b,\alpha}} \overline{\sigma}_{b,\alpha} \langle B \rangle - \overline{\sigma'^3_{b,\alpha}} \langle B \rangle \right) \right). \tag{4}$$

The subscript α refers to standard (s), standard-high (sh), or super-high (suph) scans. K-space averaging is denoted by $\langle \cdot \rangle$, and ε is:

$$\varepsilon = \langle B \rangle / \left(\overline{\sigma}_{r,s} \langle R \rangle - \overline{\sigma}_{b,\alpha} \langle B \rangle \right). \tag{5}$$

The prime indicates a fluctuation about the mean of the scan set. Note that reference scans at the standard molarity and the reference scale factor, $\overline{\sigma}_{r,s}$, were used when calculating the concentration for the standard-high and super-high

cases. A derivation of Eq. (4) is given in Appendix 1. To evaluate Eq. (4), the individual magnitude images were reconstructed, and the mean and fluctuating scale factors were computed. Then the k-space averages were evaluated. Averages such as $\left\langle \sigma'_{b,\alpha} S_\alpha \right\rangle$ were obtained by weighting the k-space data for each scan by $\sigma'_{b,\alpha,i}$. For the present levels of contamination, the $O(\varepsilon)$ and $O(\varepsilon^2)$ terms changed $\langle C_\alpha \rangle$ by less than 0.1% compared to retaining only the first term, which accounts for the average background drift.

4.4 Concentration stitching

Applying Eq. (4) to the standard scans yields a concentration field, $\langle C_s \rangle$, in the range of zero to unity. $\langle C_{sh} \rangle$ and $\langle C_{suph} \rangle$ were normalized to account for coil shading, but are not in the range of zero to unity. A matching procedure based on the low molarity data set was used to scale the high molarity cases.

The standard-high scans injected $5 \times$ molarity $CuSO_4$, so voxels from the standard data set which have $\langle C_s \rangle < 0.2$ are nominally in a linear calibration regime for the standard-high data set. An overlap region was defined as $\langle C_s \rangle \in [0.1, 0.15]$. A set of voxels in this concentration band, denoted by Ω_{sh}, were identified from the standard data and labeled in the standard-high data. The scale factor for the standard-high data was identified by minimizing the mean-square difference between standard and standard-high over Ω_{sh}:

$$\beta_{sh} = \underset{\beta_{sh}}{\mathrm{argmin}} \sum_{\Omega_{sh}} \left(\langle C_s \rangle - \beta_{sh} \langle C_{sh} \rangle \right)^2. \tag{6}$$

Results from the stitching procedure are shown in Fig. 10, which plots the standard data against the scaled standard-high data, $\beta_{sh} \langle C_{sh} \rangle$, at each voxel. The overlap
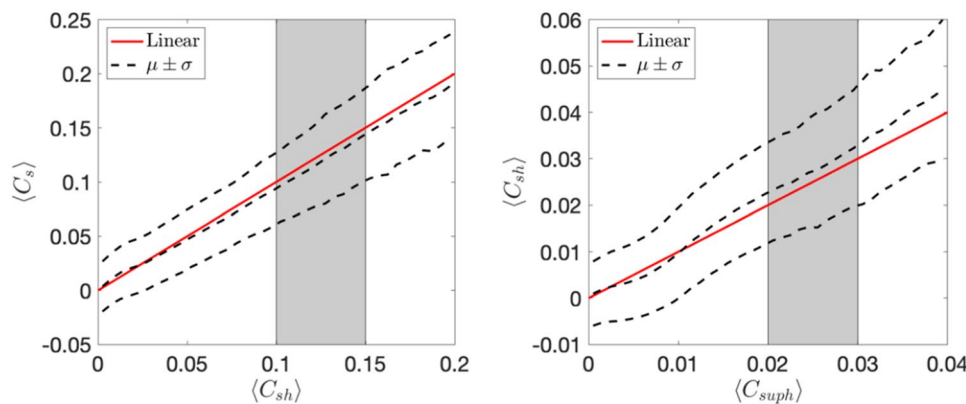

Fig. 10 Overview of the concentration stitching results for standard with standard-high (left) and standard-high with super-high (right). The concentration band used to determine the scale factor is highlighted in gray. Concentration data from the scaled, high molarity case are plotted on the abscissa and the concentration data from the low molarity case at the same voxel locations are plotted on the ordinate. The red line denotes a one-to-one linear mapping, and the black lines denote the mean and standard deviation of the low molarity data about the scaled, high molarity data

range is highlighted in gray. The standard data exhibit scatter about the standard-high data due to noise. The mean is in close agreement with the expected linear trend and the scatter is commensurate with the uncertainty estimate for the standard scan set. Note that the scatter increases towards the edge of the linear range. This is because fluctuations about the mean concentration may cause the instantaneous molarity within a voxel to be in the non-linear regime, which biases the measured concentration field. The upper bound of the overlap region was selected to reduce possible biases due to non-linear mixing, as discussed in the appendix. In general, the results were not sensitive to the range chosen.

The standard and standard-high data sets were stitched using the following formula:

$$\langle C_{s-sh} \rangle = \begin{cases} \langle C_s \rangle & ; \quad \eta > 1 \\ \eta \langle C_s \rangle + (1 - \eta)\beta_{sh}\langle C_{sh} \rangle & ; \quad \eta \in [0, 1] , \\ \beta_{sh}\langle C_{sh} \rangle & ; \quad \eta < 0 \end{cases} \quad (7)$$

where $\eta = (\beta_{sh}\langle C_{sh} \rangle - 0.1)/(0.15 - 0.1)$. Equation (7) uses the standard data at high values of concentration, linearly blends the data sets in the overlap region, and uses only the standard-high data at low concentration. Super-high data were scaled in the same manner using the scaled standard-high data. The overlap region was chosen as the set of voxels satisfying $\langle C_{s-sh} \rangle \in [0.02, 0.03]$. The result of the scaling procedure is shown in Fig. 10. The scaled super-high data, $\beta_{suph}\langle C_{suph} \rangle$, were then stitched with $\langle C_{s-sh} \rangle$ using a formula analogous to Eq. (7).

Figure 11 shows concentration contours of the unstitched and stitched data for the Flip30 case on the $z/W = 0$ plane. The stitched data include both standard-high and super-high scans. The linear blending procedure resulted in a smoothly varying concentration field. The noise was significantly reduced downstream of injection where the high molarity scans were incorporated. This is especially evident in the freestream above the injected fluid. The plume boundary is better resolved with the stitched data set.

Line plots comparing the stitched and unstitched data from the Flip30 case are shown in Fig. 12. The shaded bands represent 95% confidence intervals computed from the statistical method described in Sect. 4.5 and have been median filtered for clarity. Both data sets and their uncertainty are the same for $C > 0.15$. The stitched profiles pass through the uncertainty bands of the unstitched data throughout the overlap regions and down to zero concentration. It is evident from the line plots that the uncertainty in the stitched data is significantly reduced and that regions of zero concentration are more easily demarcated.
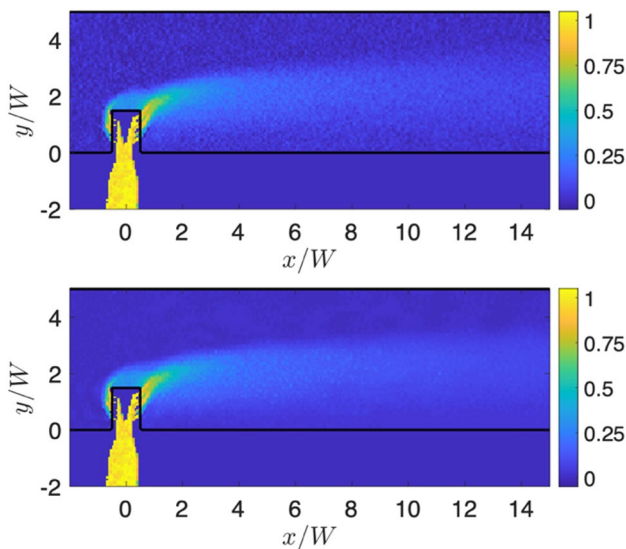

Fig. 11 Comparison of unstitched (top) and stitched (bottom) data on the $z/W = 0$ plane
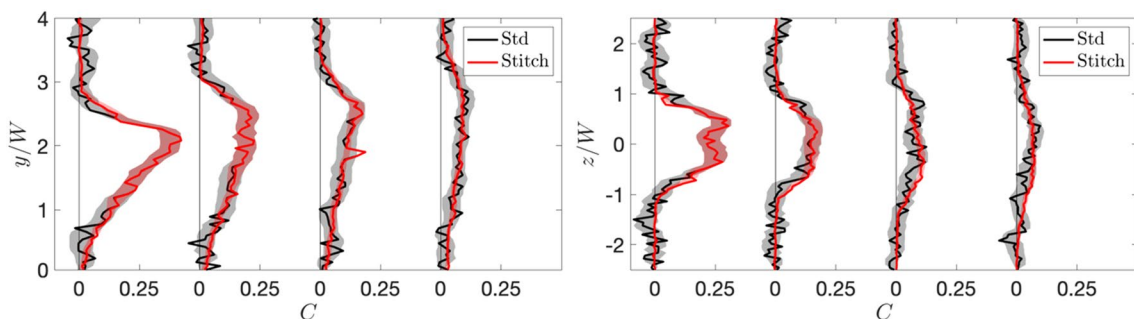

Fig. 12 Line plots comparing the unstitched and stitched concentration data at the streamwise locations $x/W = 2, 4, 8$, and 12. Vertical profiles at the $z/W = 0$ plane are shown in the left figure, and horizontal profiles in the $y/W = 1.5$ plane are shown in the right figure. The shaded bands denote 95% confidence intervals
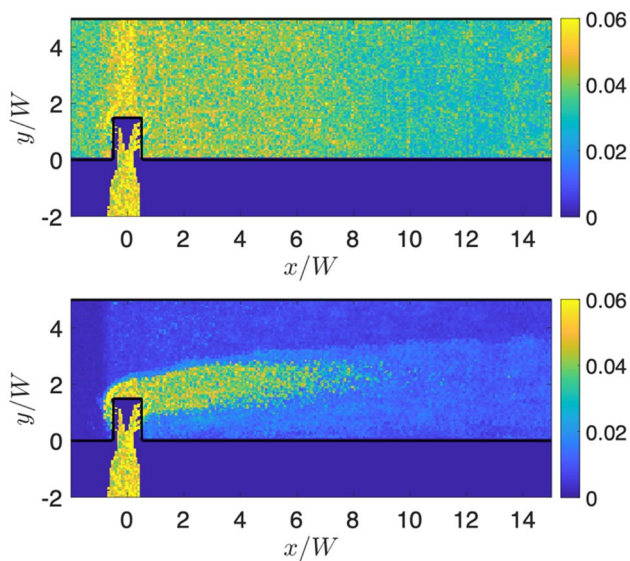
Fig. 13 Absolute uncertainty for the unstitched data (top) and the stitched data (bottom) on the $z/W = 0$ plane

Fig. 14 Relative uncertainty for the unstitched data (top) and the stitched data (bottom) on the $z/W = 0$ plane. Freestream fluid with a concentration below 0.01 has been blanked using the stitched data set

4.5 Measurement uncertainty for advanced MRC technique

The measurement uncertainty for the stitched data was computed using the statistical approach described in Sect. 3.2.5. To apply the statistical method to the stitched data, individual fields were obtained from Eq. (1) for each standard, standard-high, and super-high scan using real-space averages instead of k-space averages. The variance of these scan sets was then computed, the uncertainty was propagated through Eq. (7) using a sum of squares and 95% confidence intervals were assigned using Student's t distribution. This method gives accurate uncertainty bounds, because Fig. 9 shows that k-space averaging reduces bias from rectified noise, but does not greatly change the scatter about the local signal mean.

Figure 13 shows the uncertainty field on the $z/W = 0$ plane for the stitched and unstitched data, using the Flip30 case as an example. The uncertainty of the unstitched data varies from about 3–5% of the injected concentration. The highest uncertainty is near the injector where turbulent dephasing is most significant and decreases downstream. Note that the uncertainty is nearly uniform in the y-direction. Incorporating the high molarity scans decreases the uncertainty significantly where the blending is applied. In particular, the uncertainty decreases with decreasing concentration to below 1% of the injected concentration at the edge of the plume.

Figure 14 plots the relative uncertainty, defined as the confidence interval divided by the local mean concentration. Areas with mean concentration below 0.01 have been blanked for clarity. Islands of noise in the freestream were removed by eliminating voxels with $C \geq 0.01$ that were
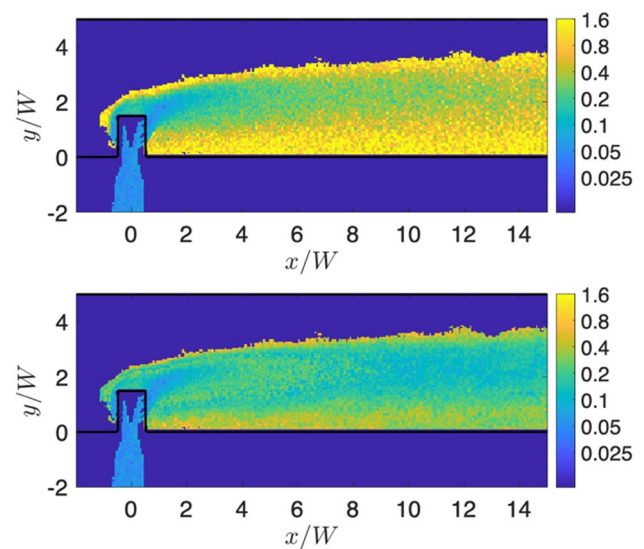
disconnected from the main plume. The relative uncertainty of the unstitched data increases significantly with decreasing concentration, because the absolute uncertainty is approximately constant. The largest values indicate uncertainty greater than 100% of the mean concentration, implying that low concentration fluid cannot be distinguished from freestream fluid. The stitched data achieve a more uniform distribution of relative uncertainty between 10 and 20% in the wake of the building. The largest relative uncertainty is about 50% of the local concentration at the bottom wall of the test section, but this is still low enough that the $CuSO_4$ solution can be distinguished from pure water.

Additional biases exist which were not accounted for by the statistical procedure. These include the same sources identified in Sect. 3.2.5 for the baseline MRC method. The advanced method introduces a new source of bias through the β-factors used to stitch the data sets. The high molarity scans injected 5 and 25 times the reference concentration, so it was expected that the factors would be close to $\beta_{sh} = 0.2$ and $\beta_{suph} = 0.04$. It was found that $\beta_{sh} = 0.22$ and 0.20 for the Flip30 and Flip55 scans, respectively. The super-high scale factor was $\beta_{suph} = 0.055$ for the Flip30 scans. Deviations from the nominal factors can be due in part to hardware drift, in which case the measured factor gives an appropriately normalized concentration field (it can be shown that background subtraction and normalization by a multiplicative factor give the correct concentration field assuming a linear calibration curve).

Alternatively, the discrepancy could be due to intermittent mixing of high molarity fluid in Ω_{sh} and Ω_{suph}. In this case, the average signal magnitude is less than the signal at

the average molarity due to the non-linearity of the calibration curve, leading to a larger scale factor. If the number of voxels with non-linear mixing is a large fraction of Ω_{sh} and Ω_{suph}, then β will be biased and the concentration will be overestimated. Otherwise, β will be unbiased but the voxels with non-linear mixing will have underestimated concentration. The concentration band used for blending data sets was selected to balance the possibility of bias against the benefit of reduced uncertainty. Considering the difference between the experimentally obtained scale factors and their nominal values, the bias from stitching standard and standard-high is less than 10% of the local concentration and, therefore, negligible compared to other uncertainties (e.g., an uncertainty of ± 0.005 at $C = 0.05$). The bias from stitching in the super-high data is about 40% of the local concentration and, therefore, may be important at low concentration.

Given the fact that the deviation of β from its nominal value can increase with the number of stitching recursions, it is reasonable to ask how many data sets can be stitched before a bias error of 100% of the local concentration is incurred. To estimate this maximum number of stitching recursions, we considered a simplified model for the non-linear mixing bias. Assume that the measured signal is biased low at the concentration stitching band for each recursion level, but that the signal is unbiased at lower concentrations. This is a reasonable assumption, because very dilute regions of the plume are likely the most well-mixed. Under this assumption, let the ratio of the unscaled concentrations between each level at the stitching band be $C_k/C_{k+1} = \gamma(1 + X)$, where k denotes the level of stitching. The factor γ is the ratio of the injected molarities and is assumed constant (e.g., $\gamma = 0.2$ in the present experiments). X is the bias error that causes the scale factor computed through the optimization procedure to differ from the nominal scale factor, and is assumed constant across levels for simplicity. It can be shown by applying Eq. (7) recursively that the maximum number of stitching levels, N, is approximately $N \approx 1/X$. As an example relevant to the present experiments, if $X = 0.25$, then $N = 4$, $\beta_{sh} = 0.25$, and $\beta_{suph} = 0.06$,. However, it should also be noted that the bias is multiplicative, so that fluid with a dilute concentration can still be distinguished from zero concentration, irrespective of the amount of bias error.

In theory, the concentration band for matching the data sets should be chosen to exclude voxels with non-linear mixing, or a secondary mask could be applied. However, the concentration fluctuations are unknown in practice. Appendix 2 presents a mixing model which quantifies measurement bias as a function of the probability distribution of concentration fluctuations to provide some intuition for this effect. Further research is required to fully characterize the uncertainty in β, because the uncertainty is expected to stem from a variety of sources (including but not limited to non-linear mixing bias) that also depend on the stitching level. This will be a topic of future work.

5 Results and discussion

The preceding sections showed that the advanced MRC technique greatly reduces the measurement uncertainty in regions of the plume with $C < 0.15$. In this section, the stitched data sets are used to identify several unique features of the plume which were difficult to discern with the baseline methodology.

Figure 15 plots vertical and spanwise profiles of concentration for the Flip30 and Flip55 cases. The stitched data show remarkable agreement, lending further support to the use of low flip angle scans for cases where property variations must be minimized. The point of maximum concentration moves upward and the plume width grows with increasing downstream distance. Injected fluid does not reach the top or side walls of the test section by 12 building widths downstream of the origin. Despite the fact that fluid is injected with a significant vertical component of momentum, turbulence in the wake rapidly mixes fluid
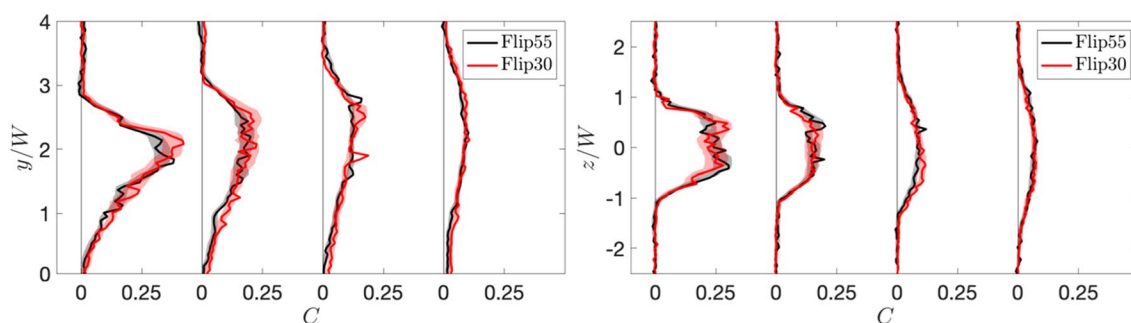

Fig. 15 Profiles of stitched concentration data at the streamwise locations $x/W = 2, 4, 8$, and 12 (repeated from Fig. 12 for clarity). Vertical profiles at the $z/W = 0$ plane are shown in the left figure, and horizontal profiles in the $y/W = 1.5$ plane are shown in the right figure. The shaded bands denote 95% confidence intervals

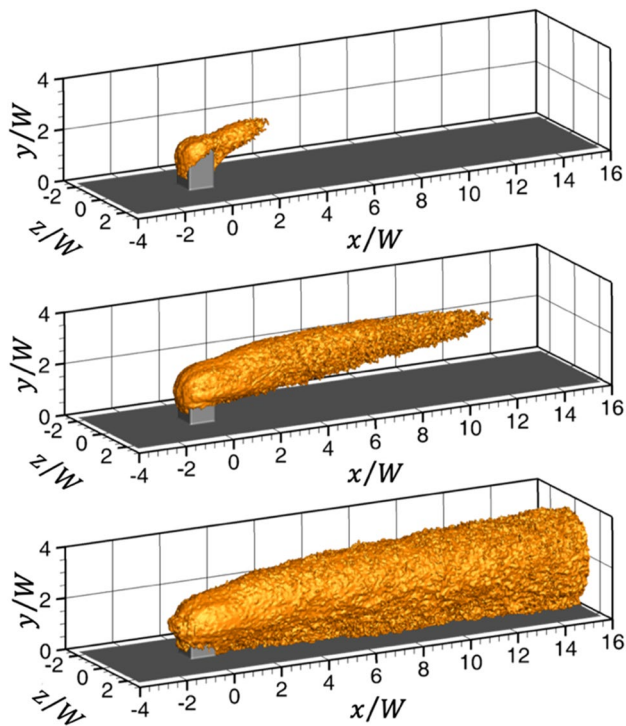**Fig. 16** Concentration isosurfaces from the 30° flip angle stitched data set at $C = 0.3$, 0.1, and 0.02 (top, middle, and bottom)

in the negative y-direction. By $x/W = 12$, there is a dilute amount of injected fluid at the bottom wall of the test section. The concentration of this fluid is less than 2% and could not have been resolved with only the baseline MRC technique (c.f. Fig. 8).

The concentration field obtained using MRC is three dimensional. The spatial structure of the full 3D concentration distribution can be analyzed by plotting isosurfaces of concentration. Figure 16 shows isometric views of the isosurfaces for three different concentrations. Islands of noise in the freestream were removed by eliminating voxels with concentration greater than or equal to the isosurface of interest that were disconnected from the main plume. The fluid injected from both sides of the building mixes rapidly with the freestream fluid. This process is most pronounced for fluid exiting the upstream side of the building, which has fallen almost entirely below $C = 0.3$ before intersecting fluid injected from the downstream face. The entire plume quickly turns to align with the freestream flow downstream of the building. Fluid with concentration greater than $C = 0.3$ is confined to within the width of the building and does not extend beyond $x/W = 2$ downstream of the origin.

High-concentration fluid from the upstream face predominantly travels over the top of the building. However, examination of the $C = 0.1$ and 0.02 isosurfaces show that lower concentration fluid is advected around the side of the building in line with the bottom row of holes. Downstream,

very low concentration fluid is transported to the bottom wall of the test section as described above.

6 Conclusions

Magnetic resonance concentration measurements (MRC) have been developed and improved for nearly 10 years. The technique produces three-dimensional (3D), mean concentration data for the turbulent mixing of two fluid streams. MRC leverages widely available, research grade medical imaging equipment and can be applied to arbitrarily complex geometries additively manufactured with MRI-compliant materials. Typical geometries can be tens of centimeters in size and scanned with sub-millimeter resolution to give data sets with $O(10^6)$ points on a volumetric Cartesian grid. The highly detailed, 3D data sets are useful for design and analysis of complex turbulent flows, and for validation of numerical simulation data. Despite its advantages, MRC has several limitations. Turbulence statistics cannot be measured with current pulse sequences, the data are not wall-resolved, and measurement uncertainty is typically near 5% of the injected concentration.

The purpose of the present work was to address issues related to measurement uncertainty in three ways. First, best practices for conducting MRC measurements were defined, including details of the experimental set-up, scan parameters, calibration procedure, scan types (reference, background, and standard), and measurement uncertainty. These best practices were termed the baseline methodology. Second, results obtained using a low flip angle were validated against the baseline method. Low flip angle allowed for reduced $CuSO_4$ concentrations and, therefore, minimized fluid property differences. Third, an advanced MRC technique was developed to greatly reduce the measurement uncertainty at low concentration.

The advanced technique improved the baseline combination of reference, background, and standard scans by introducing a set of standard-high scans, during which high molarity fluid was injected. A k-space averaging procedure was implemented, and the standard-high data were combined with the baseline data set via a stitching step. The advanced technique was repeated recursively using super-high scans to further reduce measurement uncertainty. The $CuSO_4$ molarity and flip angle can be selected to optimally balance reduced uncertainty and fluid property differences for a given application. Uncertainty can be reduced below 1% for low concentration data, allowing mapping of dilute edges of a concentration plume, and without drastically increasing the overall duration of the experiment.

The advanced MRC method was used to measure the scalar dispersion in the wake of an isolated building and was compared to the baseline method. The measurement uncertainty was reduced to below 1% of the injected concentration and

increased the number of scans by less than a factor of 2. The stitching technique reduced uncertainty specifically in regions of low concentration and yielded a relative uncertainty map which was approximately constant. Both the advanced MRC technique and low flip angle scans agreed with results obtained using the baseline method to within experimental uncertainty. The advanced technique revealed regions of dilute yet non-zero concentration very near the wall in the wake of the building which could not be detected using the baseline method. Additional aspects of the 3D concentration field were described. It is anticipated that the establishment of best practices and improvements to the MRC technique in the present work will make MRC accessible to a wider user-base and broaden its applicability to flows where measurement of dilute concentration is required.

Appendix 1: Derivation of the concentration equation for *k*-space averages

Equation (4) is obtained by decomposing the background scale factor into a mean and fluctuation for each scan ($\sigma_{b,\alpha,i} = \overline{\sigma}_{b,\alpha} + \sigma'_{b,\alpha,i}$), Taylor expanding up to second order in the factor ε, and replacing ensemble averages by *k*-space averages. Fluctuations in the reference scale factor were negligibly small, because the injection line is not contaminated by mixed fluid. Equation (4) assumes that $\langle B \rangle \approx \overline{B}$ and $\langle R \rangle \approx \overline{R}$, and that the scale factors computed from the individual magnitude images are appropriate for scaling the *k*-space data. The former assumption is accurate, because bias from Rician noise was negligible below the reference molarity. The scale factor assumption is justified for ROI, 0, because it is located upstream of injection and unaffected by noise, as shown in Fig. 9. The reference scale factor was weakly affected by rectified noise around the injector. The scale factor $\overline{\sigma}_{r,s}$ was also computed from the *k*-space averaged data for comparison. The relative change in $\langle C_\alpha \rangle$ was less than 1% for Flip30 and less than 3% for Flip55, so bias in the reference scale factor is negligible, especially at low concentration.

Appendix 2: Bias error due to non-linear mixing

The procedure to stitch data from standard-high scans assumes that the fluid molarity at each voxel in Ω_{sh} is in a linear portion of the calibration curve ($M < M_{\text{ref}}$). Those voxels are identified so that the mean concentration satisfies this assumption, but the instantaneous molarity can exceed the linear regime due to turbulent fluctuations. In this case—termed non-linear mixing—a bias error is incurred, because the mean signal magnitude is not equal to the signal magnitude at the mean concentration. Specifically, the signal is a concave function of the $CuSO_4$ molarity, $f(M)$, and Jensen's inequality gives:

$$\langle s \rangle \leq f(\langle M \rangle). \tag{8}$$

This appendix presents a mixing model to quantify bias error due to non-linear mixing as a function of the probability distribution of concentration fluctuations. Data from the Flip30 case for standard-high stitching are taken as an example, but the higher flip angle and super-high data are similarly affected.

The calibration data from the Flip30 case are modeled using a fourth-order polynomial of the form:

$$s = f(M/M_{\text{ref}}) = d_4(M/M_{\text{ref}})^4 + d_3(M/M_{\text{ref}})^3$$
$$+ d_2(M/M_{\text{ref}})^2 + d_1(M/M_{\text{ref}}) + d_o, \tag{9}$$

where the d_k coefficients are determined from a least-squares fit. Figure 17 plots the data and fitted curve, showing the deviation from linearity at high concentrations. The data are normalized using M_{ref}, so that the end of the linear range is $M/M_{\text{ref}} = 1$. The fluid injected for standard-high scans corresponds to $M/M_{\text{ref}} = 5$, and the upper bound of Ω_{sh} is $M/M_{\text{ref}} = 0.75$. Concentration fluctuations are modeled using the beta distribution to bound the concentration between zero and the injected molarity ($0 \leq M/M_{\text{ref}} \leq 5$) and to account for large fluctuations. The beta distribution is given by:
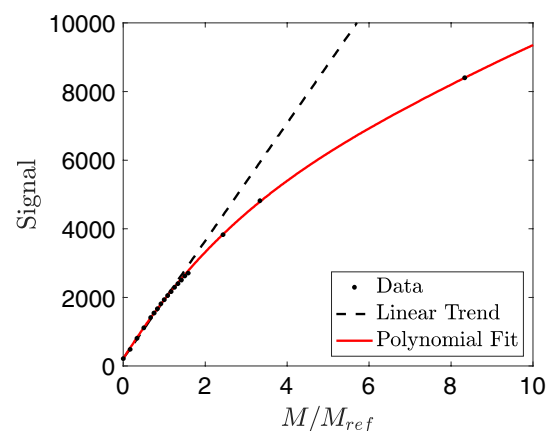

Figure 17 Polynomial fit to the Flip30 calibration data. The abscissa is normalized by the reference molarity for standard scans: $M_{\text{ref}} = 0.006\,\text{M}$

Figure 18 Parameter regime for unbiased concentration stitching. Left: regime map showing the $E < 0.01$ boundary (gray line) and the $\langle C \rangle < 0.15$ boundary (black line). The set K is highlighted in blue. Right: probability distributions of molarity normalized by the reference molarity at points A, B, and C indicated on the regime map
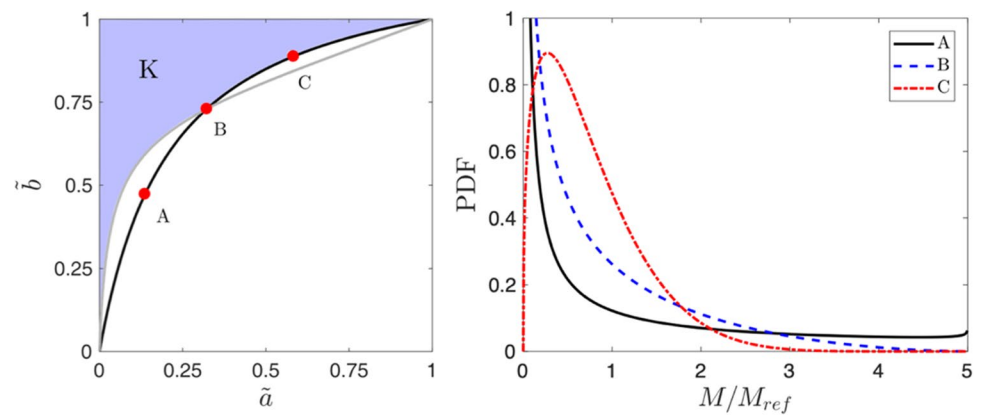
$$p(\zeta) = (\zeta)^{a-1}(1-\zeta)^{b-1}\Gamma(a+b)/\Gamma(a)\Gamma(b), \tag{10}$$

where $\zeta \equiv M/5M_{\mathrm{ref}} \in [0,1]$, $a \in [0,\infty)$, $b \in [0,\infty)$, and $\Gamma(\cdot)$ is the gamma function. To simplify the presentation of results, we define the following parameters: $\tilde{a} \equiv 1 - 1/(1-a) \in [0,1]$ and $\tilde{b} \equiv 1 - 1/(1-b) \in [0,1]$.

The measured signal magnitude, $\langle s \rangle$, is obtained by averaging equation (9) with respect to (10). The standard-high concentration is computed using the assumption of linearity:

$$\langle C_{\mathrm{sh}} \rangle = (\langle s \rangle - f(0))/(f(1) - f(0)). \tag{11}$$

The normalized concentration is then given by $\beta_{\mathrm{sh}}\langle C_{\mathrm{sh}} \rangle$. For the present purpose, we set $\beta_{\mathrm{sh}} = 0.2$ (ideal scaling) and define the error with respect to the true average concentration as:

$$E = \left| \beta_{\mathrm{sh}}\langle C_{\mathrm{sh}} \rangle - \langle C \rangle \right|. \tag{12}$$

Note that $\langle C \rangle$ is the mean of the beta distribution, but in practice it is determined from the standard scans (e.g., $\langle C_s \rangle$).

The model is used to construct a regime diagram for unbiased stitching, defined as the union of points in the $\tilde{a} - \tilde{b}$ parameter space with mean concentration in the stitching range and an acceptable level of error. Specifically, the unbiased regime is the set:

$$\mathrm{K} = \left\{ (\tilde{a}, \tilde{b}) : \langle C \rangle \le 0.15 \text{ and } E \le 0.01 \right\}. \tag{13}$$

An error tolerance of 1% is chosen to be consistent with the target for the advanced MRC technique. Figure 18 shows the unbiased regime and plots several concentration PDFs along the $\langle C \rangle = 0.15$ boundary to illustrate the types of fluctuations producing high and low measurement bias. The PDF for point A shows the expected result that fluctuations of very high molarity fluid produce measurement bias that exceeds the reduction in uncertainty due to improved signal-to-noise ratio. However, points B and

C illustrate that intermittent fluctuations of high molarity fluid are tolerable. The width of the probability distribution can be large, and instantaneous molarities can exceed the linear range by a factor of two to three provided that they occur infrequently. In general, the bias error will be less than 1% if $\tilde{b} \gtrsim 0.75$ and $\tilde{a} \le 0.15\tilde{b}/(1 - 0.85\tilde{b})$. These bounds can be used as guidelines to identify regions of potentially high measurement bias when the concentration fluctuations are qualitatively known.

References

Benson MJ, Elkins CJ, Mobley PD et al (2010) Three-dimensional concentration field measurements in a mixing layer using magnetic resonance imaging. Exp Fluids 49:43–55

Benson MJ, Elkins CJ, Yapa SD et al (2012) Effects of varying Reynolds number, blowing ratio, and internal geometry on trailing edge cutback film cooling. Exp Fluids 52:1415–1430

Benson MJ, Wilde N, Brown A, Elkins CJ (2019) Detailed magnetic resonance imaging measurements of a contaminant dispersed in an Oklahoma City model. Atmos Environ. https://doi.org/10.1016/j.atmosevn.2019.117129

Bogard DG, Thole KA (2006) Gas turbine film cooling. J Propul Power 22:249–270

Borup DD, Fan D, Elkins CJ, Eaton JK (2019) Experimental study of periodic free stream unsteadiness effects on discrete hole film cooling in two geometries. J Turbomach 141:061006

Brockhinke A, Andresen P, Kohse-Hoinghaus K (1995) Quantitative one-dimensional single-pulse multi-species concentration and temperature measurement in the lift-off region of a turbulent H2/air diffusion flame. Appl Phys B 61:533–545

Coletti F, Benson MJ, Ling J, Elkins CJ, Eaton JK (2013) Turbulent transport in an inclined jet in crossflow. Int J Heat Fluid Flow 43:149–160

Cottereau MJ, Marie JJ, Desgroux P (1989) On the accuracy of laser methods for measuring temperature and species concentration in reacting flows. In: Borghi R, Murthy SNB (eds) Turbulent reactive flows. Springer, New York, pp 169–194

Crimaldi JP (2008) Planar laser induced fluorescence in aqueous flows. Exp Fluids 44:851–863

Dimotakis PE (2005) Turbulent mixing. Annu Rev Fluid Mech 37:329–356

Dunnmon J, Sobhani S, Wu M, Fahrig R, Ihme M (2017) An investigation of internal flame structure in porous media combustion via X-ray computed tomography. Proc Combust Inst 36:4399–4408

Elkins CJ, Alley MT (2007) Magnetic resonance velocimetry: applications of magnetic resonance imaging in the measurement of fluid motion. Exp Fluids 43:823–858

Escoda CM, Long MB (1983) Rayleigh scattering measurements of the gas concentration field in turbulent jets. AIAA J 21:81–84

Golnabi H (2006) Precise CCD image analysis for planar laser-induced fluorescence experiments. Opt Laser Technol 38:152–161

Haacke ME, Brown RW, Thompson MR, Venkatesan R (1999) Magnetic resonance imaging: physical principles and sequence design. Wiley-Liss, New York

Ling J, Coletti F, Yapa SD, Eaton JK (2013) Experimentally informed optimization of turbulent diffusivity for a discrete hole film cooling geometry. Int J Heat Fluid Flow 44:348–357

Lozan A, Yip B, Hanson RK (1992) Acetone: a tracer for concentration measurements in gaseous flows by planar laser-induced fluorescence. Exp Fluids 13:369–376

McGibney G, Smith MR, Nichols ST, Crawley A (1993) Quantitative evaluation of several partiall Fourier reconstruction algorithms used in MRI. Magn Reson Med 30:51–59

Milani PM, Gunady IE, Ching DS, Banko AJ, Elkins CJ, Eaton JK (2019) Enriching MRI mean flow data of inclined jets in crossflow with Large eddy simulation. Int J Heat Fluid Flow 80:108472

Nishimura DG (2010) Principles of magnetic resonance imaging. Stanford University, Stanford

Parmar ML, Thakur RC (2006) Effect of temperature on the viscosities of some divalent transition metal sulphates and magnesium sulphate in water and water + ethylene glycol mixtures. Indian J Chem 45A:1631–1637

Penner SS, Jerskey T (1973) Use of lasers for local measurement of velocity components, species densities, and temperatures. Annu Rev Fluid Mech 5:9–30

Ryan KJ (2016) Three-dimensional velocity and concentration measurements of turbulent mixing in discrete hole film cooling flows. PhD Thesis, Stanford University

Ryan KJ, Bodart J, Folkersma M, Elkins CJ, Eaton JK (2017) Turbulent scalar mixing in a skewed jet in crossflow: experiments and modeling. Flow Turbul Combust 98:781–801

Sayles EL, Eaton JK (2016) Validation of magnetic resonance concentration measurements with adiabatic wall temperature measurements. Exp Fluids 57:193

Scheck JF (1996) The role of magnetic susceptibility in magnetic resonance imaging: MRI magnetic compatibility of the first and second kinds. Med Phys 23:815–850

Shim G, Prasad D, Elkins CJ et al (2019) 3D MRI measurements of the effects of wind direction on flow characteristics and contaminant dispersion in a model urban canopy. Environ Fluid Mech 19:851–878

Sini JF, Anquetin A, Mestayer PG (1996) Pollutant dispersion and thermal effects in urban street canyons. Atmos Environ 30:2659–2677

Stein AF, Draxler RR, Rolph GD, Stunder BJB, Cohen MD, Ngan F (2015) NOAA's HYSPLIT atmospheric transport and dispersion modeling system. Bull Am Meteorol Soc 96:2059–2077

Yapa SD (2015) Turbulent coolant dispersion in the wake of a turbine vane trailing edge. PhD Thesis, Stanford University

Yapa SD, D'Atri JL, Schoech JM et al (2014) Comparison of magnetic resonance concentration measurements in water to temperature measurements in compressible air flows. Exp Fluids 55:1834

Yapa SD, Elkins CJ, Eaton JK (2015) Quantitative MRI measurements of hot streak development in a turbine vane cascade. Volume 5B: heat transfer. ASME, p V05BT12A021

Zhang L, Baltz M, Pudupatty R, Fox M (1999) Turbine nozzle film cooling study using the pressure sensitive paint (PSP) technique. In: AME 1999 international gas turbine and aeroengine congress and exhibition. American Society of Mechanical Engineers